Direct time-frequency response of electronic coherences in assemblies of colloidal CdSe quantum dot dimers probed at room temperature by 2-dimensional electronic spectroscopy

James R. Hamilton[1], Edoardo Amarotti[2,*], Carlo N. Dibenedetto[3,4], Marinella Striccoli[3] R.D. Levine[5], Elisabetta Collini[2], F. Remacle[1**]

1 Department of Theoretical Physical Chemistry, University of Liège, B4000 Liège, Belgium

2 Department of Chemical Sciences, University of Padova, Padova, Italy.

3 CNR-IPCF SS Bari, c/o Chemistry Department, University of Bari Aldo Moro, Bari, Italy

4 Chemistry Department, University of Bari Aldo Moro, Bari, Italy

5 The Fritz Haber Research Center for Molecular Dynamics and Institute of Chemistry, The Hebrew University of Jerusalem, Jerusalem 91904, Israel

* Present address: Division of Chemical Physics and NanoLund, Lund University, P.O. Box 124, Lund 22100, Sweden

** Corresponding author, fremacle@uliege.be

Abstract

The advantages of the directly measured time-frequency maps are discussed as a useful representation of the coherent output in a 2 dimensional electronic spectroscopy (2DES). We demonstrate the theory by a detailed application to the fast femtosecond beatings of a wide variety of electronic coherences in dimers of size-dispersed (9%) 3nm quantum dots (QDs). The observed and computed results can be consistently characterized directly in the time-frequency domain by probing the polarization in a 2DES set-up. Experimental and computed time-frequency maps are found in very good agreement and several electronic coherences are characterized at room temperature in solution before extensive dephasing due to the size-dispersion kicks in. As compared to the frequency-frequency maps that are commonly used in 2DES, the time-frequency maps allow for exploiting electronic coherences without additional post processing and with fewer 2DES measurements of polarization. Towards quantum technology applications, we also report on the modeling of the time-frequency photocurrent response of these electronic coherences, which opens the way to integrating QD devices with classical architectures thereby enhancing the quantum advantage of such technologies for parallel information processing at room temperature.

Introduction

Semi-conducting nanoparticles, or quantum dots (QDs) are a promising hardware for a wide variety of quantum technologies[1-7]. Recently, we proposed to exploit the femtosecond fast beating electronic coherences in small few-nm QDs and QD dimers for implementing quantum parallel information processing at room temperature[8-11], using electronic coherences as logic variables. Our scheme offers a significant quantum advantage as for a set of N coupled quantum states, N^2 -1 coherences can be used to process information in parallel.[8, 12]

In previous joint theoretical-experimental studies[7, 13-15] we reported how electronic coherences could be observed and tuned in ensembles of small (mean diameter $\overline{D}$ = 2.5 to 3 nm), size dispersed (σ = 5% to 9%), CdSe QDs and QD quasi-homodimers (Figure 1 (a,b)) addressed in a 2-dimensional electronic spectroscopy (2DES) set-up. In this set-up, the polarization response is measured as a function of the first two delay times, T_1 and T_2 and directly in the frequency domain, ω_3, of the third delay time, T_3, using a CCD camera, see Figure 1(c). A Fourier transform along the first delay time, T_1, brings the maps into the frequency domain, ω_1 and allow retrieving the conventional 2DES response as a function of (ω_1, T_2, ω_3), as shown in Figure 1(f). [5, 16-18] A good agreement was found between the computed and experimental coherence responses of small ≈ 3 nm QDs and QD dimers along T_2 traces of points on the frequency (ω_1, ω_3) maps[13-15].

The (ω_1 , ω_3) frequency maps of (ω_1, T_2, ω_3) response provide ((ω_1^i, ω_3^j) coordinates for coherences between pairs of excited electronic states (*i,j)* evolving along T_2, where ω_1^i corresponds to the excitation of state *i*, $\omega_1^i = \omega_i - \omega_{GS}$ and ω_3^j is the emission from state *j*, $\omega_3^j = \omega_j - \omega_{GS}$. Bringing T_1 to the frequency domain requires however a large sampling of this delay time as well as computationally expensive FFT post-processing.[19] Here, we show by comparing experimental and computed data for the BOXCARS set-up that the electronic coherences can be equally accurately probed along T_2 traces in time-frequency (T_1, ω_3) polarization maps, which requires a smaller number of 2DES measurements and less post-processing. In (T_1,ω_3) time-frequency maps, coherences along T_2 are only partially resolved along ω_3. Then there can be several coherences between excited states that beat along T_2 at a specific address (T_1, ω_3) in the map. These are all the coherences (*i,j*) that involve an excited state *j* that emits at the frequency $\omega_3^j = \omega_j - \omega_{GS}$. We show that by measuring a single point in the (T_1, ω_3) time-frequency maps one can therefore characterize a family of coherences that beat along T_2, or address simultaneously all these coherences for parallel quantum information processing.

The ability to measure electronic coherences in the directly measured data, without the need to compute full frequency maps, greatly enhances the potential for use of electronic coherences of QDs in room temperature quantum technologies. Towards applications to quantum information processing, a photocurrent action set-up[20-27] presents several advantages over the BOXCARS one for 2DES: it is a collinear set-up, easier to operate and the output is a photocurrent that can be easier processed and integrated with a classical computer. It is therefore of interest to investigate how electronic coherences are probed in the photocurrent response. We show computationally that the electronic coherences can also be robustly probed with the action-based photocurrent response.

Synthesis of 3 nm CdSe QDs and assembly into quasi-homodimers in solution

The colloidal CdSe QDs were prepared in solution by mixing Cadmium and Selenium precursors using a hot injection technique in presence of long alkyl chain coordinating agents.[28] Such molecules act as an organic capping layer on QD surface, helping the controlled and

quasi-epitaxial growth of the nanoparticles, allowing their dispersion in organic solvents, and preventing their aggregation. This approach allows, by controlling the growth parameters, the precursor ratio and the time and temperature of the synthesis, for preparing small, 2.5 to 3.5 nm in diameter, QDs with narrow size distributions varying from 5 to 9% in mean diameter.

Quasi-homodimers of CdSe QDs with mean diameter $\overline{D}$ = 3 nm and size distribution σ = 9% are assembled in the solution by bonding pairs of size dispersed QDs with a short ($\approx 0.5\ nm$) propanedithiol ligand, see ref [28] for details of this procedure and ref [7] for the details of the synthesis of the QD dimers used in this work. Because of the unavoidable size dispersion, the QD dimers are not identical nano-objects. A schematic representation of a QD quasi-homodimer constructed in this fashion is shown in Figure 1 (a) and a Transmission Electronic Microscopy (TEM) image of one of the dimers prepared for this work is shown in Figure 1 (b).

2DES Experimental Methods

The 2DES experiment is implemented using a fully non-collinear setup, in which three fs laser pulses in the visible range are incident upon the ensemble of QD dimers in solution from different spatial directions, fulfilling the BOXCARS phase matching conditions.[19] For results on the same $\overline{D}$ = 3 nm and size distribution σ = 9% QD dimers assembled into a solid state multilayer device, see ref [7]. The experiment probes the optical polarization of the ensemble as a function of the delay times between the pulses, or of their corresponding frequencies. By giving independent control over the delay times, the BOXCARS setup allows the signal in the different phase matching directions (PMDs) to be easily extracted. For a description of the experimental setup see ref [19] and for its details in this implementation see ref [7].

The three exciting pulses and the final signal observation are separated in time by the delay times, as defined in Figure 1 (c). The delay time, T_0, is the time interval between the arbitrary origin of the time axis, set as the center time of the Local Oscillator (LO), and the first pulse, centered at t_1. The LO is a fourth pulse used as time reference and employed for heterodyne detection.[19]

The first delay time, the excitation or coherence time (T_1), is the time separation between the first and second pulses. The second delay time, the population time (T_2), is the time between the second and third pulses and the third delay time, the rephasing or emission time (T_3), is the time between the third pulse and the observation. The time at which the measurement is performed is defined as

$$t \equiv T_0 + T_1 + T_2 + T_3 \qquad (1)$$

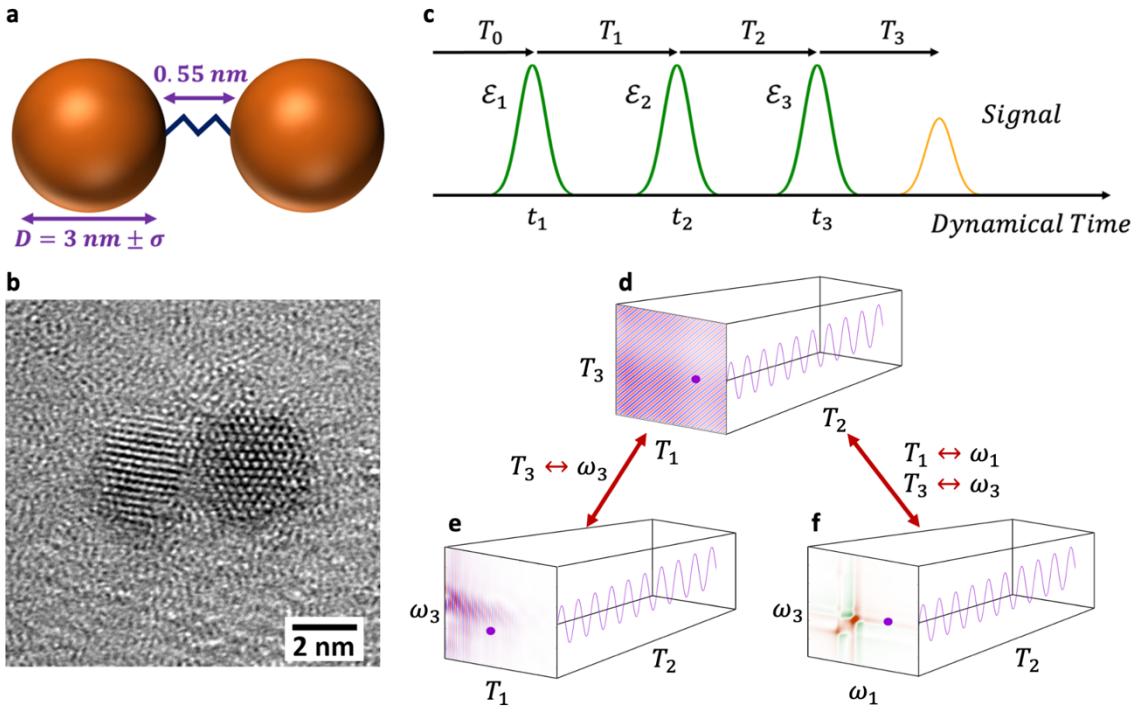

Figure 1: a) Schematic representation of a CdSe quasi-homodimer. The dimer is assembled by covalently bonding two QDs with a 0.55 nm $S(CH_3)_2S$ ligand. The QDs are drawn from an ensemble with mean diameter, $\bar{D}$, of 3 nm and size dispersion σ. b) A High Resolution Transmission Electronic Microscopy (HR-TEM) image of one of the quasi-homodimers prepared for this work. c) Time ordering of the three fs laser pulses as used in the 2DES experiment and in the modelling. d-f) Different possible representations of the final three-dimensional signal obtained after a 2DES measurements (or of modelled data). The final cube of polarisation response data can be cast as a function of: (d) the three time delays between pulses (T_1, T_2,T_3); (e) the first two delay times between pulses and the third delay in the frequency domain (T_1, T_2, ω_3). These are the data studied in this work; (f) the first and third delays in the frequency domain and the second delay in the time domain (ω_1, T_2, ω_3). This is the representation typically used when 2DES measurements are published, as was the case in ref. [12].

The polarization response from the ensemble can be measured in specific PMDs as a function of the delay times (T_1, T_2, T_3). Repeated measurements with different delays produce a "cube" of data in which the polarization in a particular PMD is stored as a function of the delay parameters. Figure 1 (d) shows the polarization in the rephasing direction in the time domain, as a function of (T_1, T_2, T_3). Each of the delay times (T_1, T_2, T_3) can be brought to the frequency domain (ω_1, ω_2, ω_3) by Fourier transform, leading to what is sometimes referred to as 3D electron spectroscopy.[29] Figure 1 (e) shows the same response as in Figure 1 (d) in the time-frequency domain (T_1, T_2, ω_3). This is the typical form of the data obtained as raw output of a BOXCARS experimental setup, such as the one used for this work. Indeed, as explained above, in a typical BOXCARS experiment, the signal is measured while scanning the time intervals T_1 and T_2, whereas the dependence on the third time interval is measured directly in the frequency domain, ω_3, by the detector.[16] For ease of interpretation, the signal is then typically Fourier Transformed along T_1[5, 16-18]. This leads to a representation of the same data as a function

of the excitation and emission frequencies and the population time (ω_1, T_2, ω_3), as shown in Figure 1 (f). Regardless of the chosen representation the electronic coherences between the excited electronic states of the QD dimers can be probed by analyzing the data in these cubes as a function of the population time, T_2, as is illustrated in Figures 1 (d) (e) and (f). Coherences in the frequency maps (ω_1, ω_3) (Figure 1 (f)) were studied in our previous work[7], while here we analyze the (T_1, ω_3) time-frequency maps.

Theoretical Methods

We model the electronic structure of each QD from two hole-one electron single particle states. These one particle electronic states are calculated using an effective mass - **k.p** Hamiltonian[30-33] constructed for CdSe using the size distribution of the ensemble (see refs. [13-15]). This approximation defines two hole-electron monoexcitons, 1S and 2S, per QD. When the laser intensity is weak enough, the formation of biexcitons, two-electron-two-hole states, can be neglected.[15, 34]

The spin $1/2$ of the hole of each pair is coupled to the *p*-type orbitals ($l = 1$) localized on the Se atoms.[35-36] These spin orbit interactions split each of the S bands into two sub-bands of states with angular momentum $L = 1 \pm 1/2$ state, $L = 1/2, 3/2$. The total orbital angular momentum, $L \pm$ the spin $1/2$ of the *s*-type orbital localized on the Cd atoms, leads to an eight-fold degeneracy of the $L = 3/2$ state and a four-fold degeneracy of the $L = 1/2$ state. These states further undergo a loss of degeneracy due to crystal field and Coulomb interactions.[33, 35-37] The $S_{3/2}$ state then forms a band of 8 fine structure (FS) singly excited electronic states, of which five are dark and three are bright, and the $S_{1/2}$ state forms a band of four FS states, of which all are bright. In this way, four bands of 24 FS states are formed per QD with energetic ordering $1S_{3/2}$, $1S_{1/2}$, $2S_{3/2}$ and $2S_{1/2}$.

When two QDs drawn from the size dispersed ensemble of monomers are covalently bonded to form quasi-homodimers, the 24 FS states of each QD are coupled by interdot electronic Coulomb interactions to create a manifold of 48 FS states per dimer. Since the two QDs in a given dimer differ slightly in size, quasi-homodimers are formed: the quasi-isoenergetic bands of each QD are split by Coulomb interdot interactions into a higher and a lower dimer band. This creates eight bands of FS singly excited states per dimer. These bands are energetically ordered as $1S^L_{3/2}$, $1S^H_{3/2}$, $1S^L_{1/2}$, $1S^H_{1/2}$, $2S^L_{3/2}$, $2S^H_{3/2}$, $2S^L_{1/2}$ and $2S^H_{1/2}$, although in dimers made from ensembles with larger $\overline{D}$ and/or size dispersion the FS states of these bands interdigitate and the bands overlap.[13, 15]

The size differences of the two QDs assembled in each quasi-homodimer mean that they do not obey the optical selection rules of exact homodimers and that all the states will share oscillator strength. Consequently, all singly excited FS states will be bright, although some FS states will be almost dark. Figure 2 (b) shows the stick spectrum calculated for the 3nm/9% ensemble averaged over an ensemble of 4000 dimers.[8, 13]

Figure 2 (a) shows the measured absorption spectra of the dimer solution along with the calculated absorption spectrum for the 3nm/9% ensemble averaged dimer where the inhomogeneous broadening due to the finite size dispersion is taken into account. This figure also shows the spectral profile of the laser pulse used for the 2DES measurements. Only the $1S^L_{3/2}$ and the $1S^H_{3/2}$ bands fall within the laser pulse energy bandwidth. Table S1 in the Supporting Information (SI) gives the calculated transition energies, inhomogeneous

broadening and corresponding dephasing times, and transition dipole moments from the ground to the $1S^{L}_{3/2}$ and $1S^{H}_{3/2}$ band FS states averaged over the 4000 dimer ensemble.

Because the laser pulses are short, several electronic states of the $1S^{L}_{3/2}$ and the $1S^{H}_{3/2}$ are excited simultaneously, which leads to a superposition of several excited FS electronic states. The electronic coherences discussed in the results section are coherences between FS excited states either within ('intra'-band) or between ('inter'-band) the $1S^{L}_{3/2}$ and $1S^{H}_{3/2}$ bands. We specifically focus on five types of coherences, labeled by the periods of their oscillations, which are governed by the energy difference of the two FS states involved. The intra-band coherences between the degenerate 4th/5th FS states and the 6th FS state, all in the $1S^{L}_{3/2}$ band, have an average frequency of $\approx 120\ cm^{-1}$. The coherences between the 3rd FS state and the degenerate 4th/5th FS states, all in the $1S^{L}_{3/2}$ band, have a frequency of $\approx 680\ cm^{-1}$. The coherences between the degenerate 1st/2nd FS states and the degenerate 4th/5th FS states, all within the $1S^{L}_{3/2}$ band, have a frequency of $\approx 850\ cm^{-1}$. The coherences between the degenerate 4th/5th FS states and the 6th FS state, all in the $1S^{L}_{3/2}$ band, have a frequency of $\approx 960\ cm^{-1}$. Finally, the inter-band coherences between the degenerate 4th/5th FS states in the $1S^{L}_{3/2}$ band and the 11th FS state in the $1S^{H}_{3/2}$ band fall at $\approx 480\ cm^{-1}$. All these coherences, both intra- and inter-band are interdot in character, due to the delocalization of the wavefunctions of the $1S$ FS states over the whole dimer.[7] The horizontal double headed arrows superimposed onto the stick spectrum, Figure 2 (b), identify these five coherences and their calculated frequencies, periods, inhomogeneous dephasing times and emission dipole strengths are given in Table S2 in the Supporting Information. Throughout this work the $120\ cm^{-1}$ coherences are labeled in red, and the $680\ cm^{-1}$, $850\ cm^{-1}$, $960\ cm^{-1}$ and $480\ cm^{-1}$ coherences in orange, green, purple and cyan respectively.

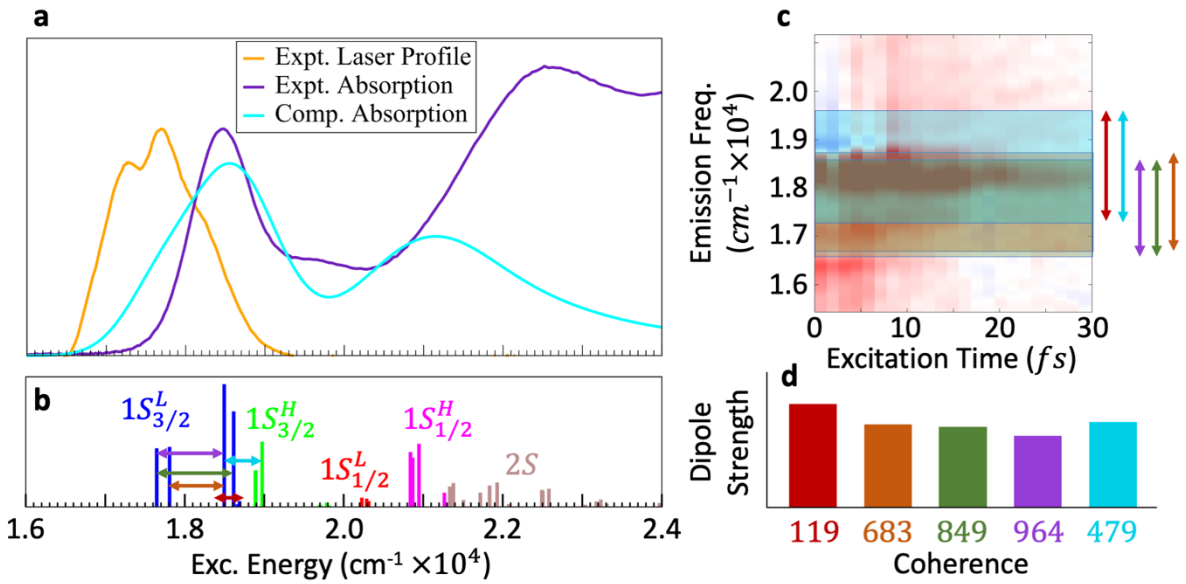

Figure 2: a) Measured (violet) and calculated (azure) absorption spectra of the QD dimers with the spectral profile of the laser pulse (orange) used for the 2DES measurement. b) Calculated stick spectrum for the averaged dimer computed from an ensemble of 4000 3nm/9% dimers. The five electronic coherences between specific electronic FS states discussed in this work are identified with horizontal double arrowed lines between these states. The colour labelling of the FS bands and coherences is used throughout. c) Inhomogeneous broadening of the 5 electronic coherences in the frequency ω_3 in the (T_1, ω_3) map. d) Emission dipole strengths of the five electronic coherences.

The size dispersion of the QD ensemble causes an inhomogeneous broadening of the energies of the transitions between electronic states, the values of which are given in Table S1 in the SI. In the time domain, the size dispersion leads to the dephasing of the coherences, which have a finite lifetime. In the (T_1, ω_3) time-frequency domain, the size dispersion therefore leads to dephasing along T_1 and to an inhomogeneous broadening of emission bands along ω_3. The inhomogeneous broadening of the bands corresponding to the five coherences on which we focus is represented as shaded areas on time-frequency (T_1, ω_3) map reported in Figure 2 (c). Traces along T_2 for points localized in a given ω_3 band on the (T_1, ω_3) map will therefore exhibit beating periods that are characteristic of coherences (*i,j*) involving an excited state *j* that emits in the range of ω_3 values specified by the inhomogeneously broadened transition frequency $(\omega_j - \omega_{GS})$.

Figure 2 (d) shows the emission dipole strengths of the same five electronic coherences. As shown in ref. [7], the rather monotonic distribution of these values results from the 9% size dispersion of the ensemble which breaks the exact homodimer limit of fully dark and bright states. The rather even distribution of dipole strengths of the five coherences means that they will appear in the T_2 traces of points on the time-frequency (T_1, ω_3) maps with commensurate strength. This is a useful feature of disordered QD quasi-homodimers for applications in quantum technologies because it means that more coherences are available for implementing information processing.

In this work the partial polarizations in specific phase matching directions are modeled using a phase modulated approach[38] which is numerically more straightforward to implement than a full simulation of the BOXCARS set-up. In the experimental BOXCARS set-up, phase modulation is not needed since the different phase matching directions are spatially separated by using a non collinear set-up. [5, 16-18] On the other hand, a phase modulation of the trains pulses is experimentally implemented in 2DES collinear set-ups that measure action observables such as fluorescence or photocurrent. [20-22, 25-26, 39-40] To simulate the polarization response as measured in the BOXCARS set-up, we compute the polarization of the ensemble of QD dimers subject to sequences of three collinear fs phase modulated laser pulses. The electric field time profile of the pulse sequence is given

$$\mathcal{E}(t) = \sum_{n=1}^{3} \mathcal{E}_n(t) \qquad (2)$$

Where $\mathcal{E}_n(t)$ is the electric field of each pulse defined as

$$\mathcal{E}_n(t) = \mathcal{E}_0 e^{\left(-\frac{(t-t_n)^2}{2\sigma_n^2}\right)} \cos\left(\omega_n t + \phi_n\right) \qquad (3)$$

In Eq. (3) $\mathcal{E}_0$ is the electric field strength, σ_n is the width of the Gaussian envelope, ω_n is the carrier frequency and t_n is the time at which the nth pulse is centered, as shown in Figure 1 (c). In all the calculations we use $\mathcal{E}_0 = 8.775 \times 10^7$ W/cm^2, $\omega_n = 2.36$ eV and $\sigma_n = 3.9\, fs$ for $n = 1, 2, 3$, in agreement with the experimental values.

We modulate the carrier envelope phase of the pulse, ϕ_n, for each set of delay times (T_1, T_2, T_3). The modulation of ϕ_n is expressed as $\phi_n \equiv 2\pi k_n u$ where $k_n \equiv m_n/L$. By choosing the constants m_n of each pulse as integer divisors of L, with $m_1 \neq m_2 \neq m_3$, after L repetitions

for u varying from 1 to L, each of the carrier envelope phases, ϕ_n, will have gone through a different number of complete cycles.

The computations are repeated for ranges of delay times (T_1, T_2, T_3), modulating the carrier envelope phases of the pulses for each set of values (T_1, T_2, T_3). In this way the polarization of the dimer ensemble is computed as a function of the delay times and phase modulation, u. The wave vector of each phase matching direction (PMD) is given as a linear combination of the m_n: $\boldsymbol{k}_l = l_1 m_1 + l_2 m_2 + l_3 m_3$, where the additional factors of u/L modulate the carrier envelope phase of the pulses. For the rephasing direction $(l_1, l_2, l_3) = \pm(-1, +1, +1)$.

The polarization of the ensemble in a particular PMD is extracted by Fourier transforming along the phase modulations, *u*, and identifying the signal by the value of $\boldsymbol{k}_l$.

$$\mathcal{P}_{\boldsymbol{k}_l}(T_1, T_2, T_3) = \sum_{u=1}^{L} P_u(T_1, T_2, T_3) \cdot e^{-\frac{i2\pi}{L} k_l u} \tag{4}$$

The polarization of the ensemble as a function of the delay times and phase modulation, $P_u(T_1, T_2, T_3)$ is calculated from the time dependent ensemble density matrix, $\boldsymbol{\rho_{ens}}$, as described in refs.[8, 13]

$$P_u(t) = Tr[\boldsymbol{\mu}\, \boldsymbol{\rho_{ens}}(t)] \tag{5}$$

Where $\boldsymbol{\mu}$ is the ensemble dipole matrix. The density matrix, $\rho_{ens}(t)$, is propagated along time, for each set of delay time and phase modulation parameters, using the ensemble Liouville approach[8, 13].

The Liouville equation for the ensemble is given by[8]

$$i\hbar \frac{\partial}{\partial t} \rho_{ens}^{nm}(t) = \sum_{ij} L_{nm,ij}^{ens} \cdot \rho_{ens}^{ij}(t) \tag{6}$$

Where L^{ens}, the ensemble Liouville matrix, is constructed from averaging the Hamiltonian matrices of the individual size-dispersed dimers over the ensemble and takes into account the size dispersion of the QDs. The ensemble Hamiltonian explicitly includes the interaction of the sequence of three laser pulses in the dipole approximation. Eq. (6) is solved numerically using the Cash-Karp Runge-Kutta method.

For a given set of delay times, (T_1, T_2, T_3), the polarization is calculated for given sets, *u*, of carrier envelope phases (ϕ_1, ϕ_2, ϕ_3) using Eq. (5) and parametrized in terms of these delay times using Eq. (1).

$$P_u(T_1, T_2, T_3) = P_u(t) \tag{7}$$

The polarization in each PMD is obtained by Fourier transform over u using Eq. (4). We focus here on the rephasing PMD. The computed data, $P_{reph}(T_1, T_2, T_3)$, are the time domain "cube" (Figure 1 (d)) and are converted into the time-frequency domain by Fourier transforming it along $T_3 \leftrightarrow \omega_3$.

$$\mathcal{P}_{reph}(T_1, T_2, \omega_3) \leftrightarrow \int e^{-i\omega_3 T_3} P_{reph}(T_1, T_2, T_3) dT_3 \qquad (8)$$

This produces a cube of data for the polarization of the ensemble in the rephasing direction in the time-frequency domain, as shown in Figure 1 (e). These computed data can be directly compared to the data measured in the BOXCARS setup in the time-frequency domain.

A rotating frame (RF)[41] is applied to the measured and calculated $\mathcal{P}_{reph}(T_1, T_2, \omega_3)$. [19] A reference frequency, ω_{ref}, is subtracted along T_1, thereby detuning the optical frequency.

$$\mathcal{P}_{reph}^{RF} = \mathcal{P}_{reph} e^{i\omega_{ref} T_1} \qquad (9)$$

In the computations, we take $\omega_{ref} \equiv \omega_n$. As shown in Figure 3, working in the RF makes the electronic coherence between excited FS states clearer by removing the fast-beating coherences between the excited FS states and the GS which have a much shorter dephasing time. This also allows for a less dense sampling in time along T_1 and T_3.

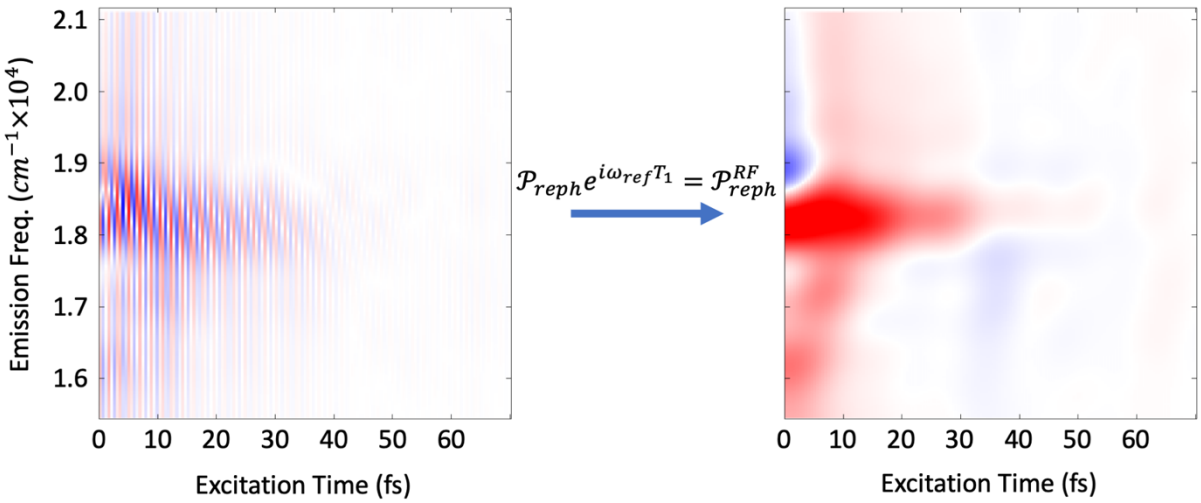

Figure 3: The rotating frame transformation is applied to measured and calculated time-frequency maps. Left) unrotated time-frequency map and right) rotated time frequency map.

Results and Discussion

Comparison of computed and experimental time-frequency polarization maps

In our previous work,[7] we showed that the electronic coherence response could be consistently characterized in BOXCARS polarization measurements of both solid-state and solution samples. Several electronic coherences between FS states in traces along T_2 and their Fourier transforms (FTs) were characterized at specifically addressed points on measured and calculated rephasing frequency maps, $\mathcal{P}_{reph}(\omega_1, T_2, \omega_3)$. Coherences were gathered in three groups, ρ_I, ρ_{II} and ρ_{III}, defined by their beating frequencies and electronic character. The group ρ_I included the intra-band coherences with low transition frequency 120 cm^{-1}. The group ρ_{II} was constituted of inter-band coherences with transition frequency 480 cm^{-1}. Finally, group ρ_{III} included the intra-band coherences with transition frequency 680 cm^{-1}, 850 cm^{-1} and 960 cm^{-1}. The low frequency group ρ_I coherences were not observed in the measured dimer solution sample, only in the dimer-solid state ensemble.

Figure 4 compares the real parts of the measured (left) and calculated (right) rephasing (T_1, ω_3) time-frequency maps at T_2 = 20 fs. In this range of T_1 values, the main signal in both maps appears at an emission frequency around $\omega_3 = 18400$ cm^{-1}. This frequency corresponds to the transition energy between the ground state and the strongest dipole FS states in the first $1S^L_{3/2}$ band. The experimental and calculated time-frequency maps are in very good agreement. The differences between the measured and calculated maps at emission frequencies below the main signal are attributable to Rayleigh scattering in the measurement.

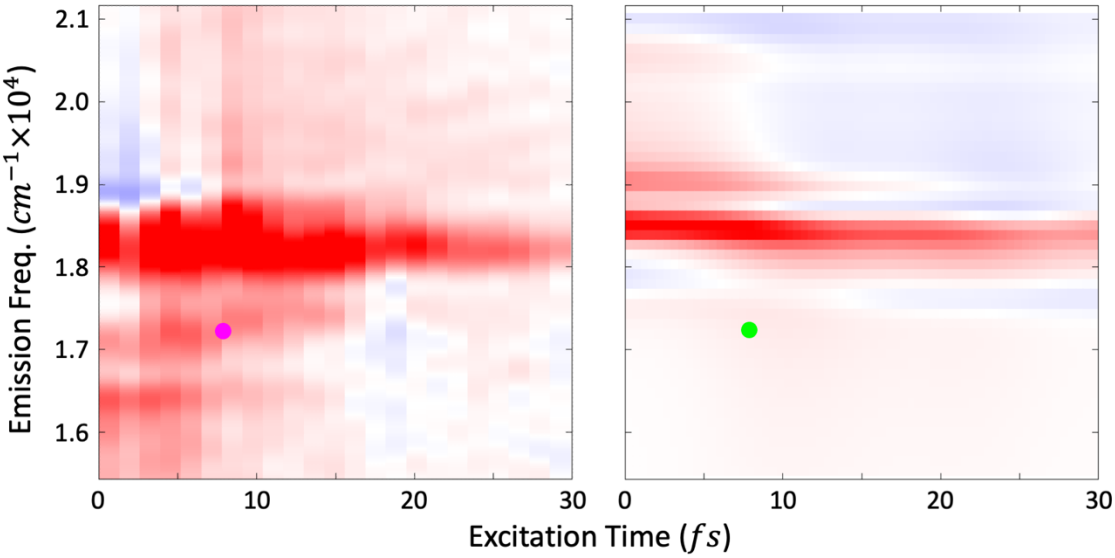

Figure 4: Left) measured and Right) calculated (T_1,ω_3) maps at T_2 = 20 fs after the rotating frame has been applied. The pink and green circles indicate the points ($T_1 = 7.8\ fs$, $\omega_3 = 17186\ cm^{-1}$) where the traces along T_2 on Figure 5 were taken.

Traces along T_2 at the points ($T_1 = 7.8\ fs$, $\omega_3 = 17186\ cm^{-1}$), indicated with pink and green dots on Figure 4, are compared on the left panel of Figure 5, and the FTs of these traces are shown on the right panel:

$$\int e^{-i\omega_2 T_2} P_{reph}(T_1, T_2, \omega_3) dT_2 \leftrightarrow \mathcal{P}_{reph}(T_1, \omega_2, \omega_3) \qquad (10)$$

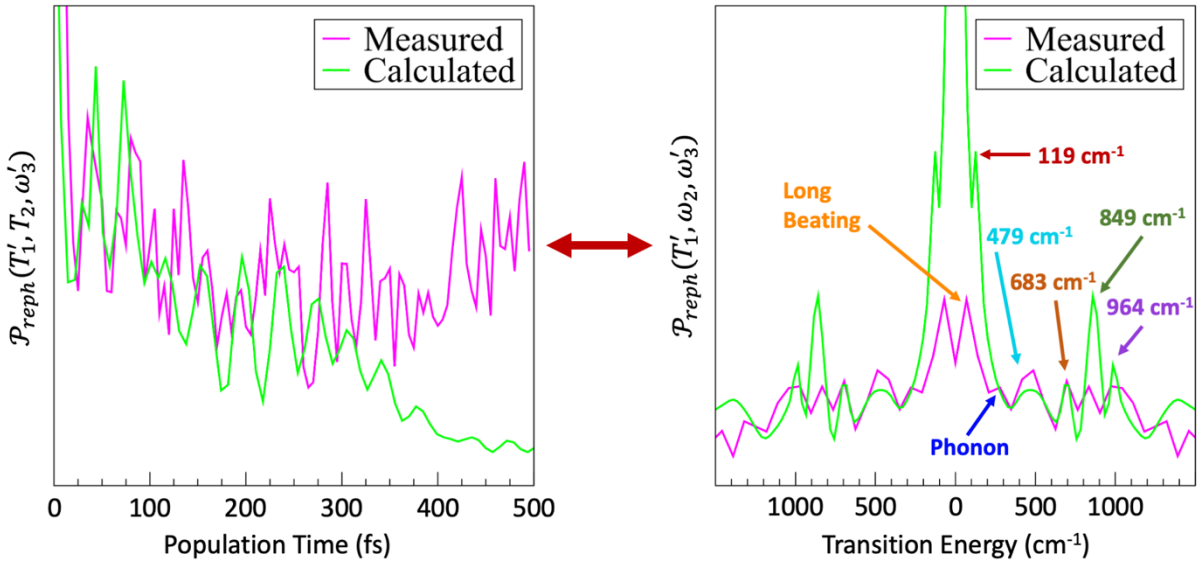

Figure 5: Left) Real part of the traces along T_2 at the points ($T_1 = 7.8\ fs, \omega_3 = 17186\ cm^{-1}$) on the measured (violet) and calculated (green) time-frequency maps. Right) FTs of the time traces.

The FTs of the traces show the characteristic beating frequencies of all the types of electronic frequencies discussed above in the measured and in the calculated FT traces. The exception to this is the 120 cm^{-1} coherence which, while it can be seen in the calculated FT, cannot be seen in the measured FT. This finding is consistent with our observations in the frequency domain.[7] While the 120 cm^{-1} coherence was observed in the measured dimer solid-state traces of the frequency maps, it was not observed in the measured dimer solution traces. The coherences with frequencies 480 cm^{-1}, 680 cm^{-1}, 850 cm^{-1} and 960 cm^{-1} appear distinctly in both the measured and calculated FTs. These coherences appear more distinctly in the measured FT on Figure 5, than in the FTs of the T_2 traces in the (ω_1, ω_3) frequency domain measured in solution.[7] A long beating can be seen in the measured T_2 trace, which is likely the acoustic phonon beating.[42] It is not present in the calculated time trace or its FT, because our model does not include the coupling to the two phonon modes. Similarly, the vibrational phonon beating can be seen in the measured time trace but not the calculated time trace.

The coherences discussed above are clearly defined in both the measured and calculated FTs in the time-frequency domain by analyzing a single trace along T_2. Producing results in this way, as opposed to using (ω_1, ω_3) frequency-frequency maps, leads to a drastic reduction in the number of the 2DES measurements needed. The ω_3 coordinate of the trace is consistent with its address in the frequency domain and depends upon the transition energies of the excited FS states involved in the coherences to the ground state. The coherences observed in Figure 5 can be found at a range of T_1 values from $2\ fs < T_1 < 10\ fs$. A clear signal is not discernable at lower values of T_1 because of the overlap between the first and the second pulses, which creates complex beating patterns. Hence intra and inter-band coherences can be found in the time-frequency maps in a small range of short T_1 values and in a range of ω_3 values which is defined by the transition energies from the FS states involved in the coherences to the GS.

The fact that the same electronic coherences can be characterized in the time-frequency domain as in the frequency-frequency domain of the 2DES experiments, and hence can be exploited in the directly measured data, is advantageous in two respects. The first is that the need for a post processing step, Fourier transforming along $T_1 \leftrightarrow \omega_1$, is removed. This yields a computational reduction of $\mathcal{O}(N_{T_1} log N_{T_1})$ where N_{T_1} is the number of measurements along T_1 . Following

the removal of the FT step, the second advantage gained is the requirement for far fewer measurements along T_1 than are required to sufficiently resolve the FT needed to obtain frequency-frequency maps. As has been discussed, measurements up to $T_1 = 10\ fs$ provide an adequate range in which the coherences can be exploited. This range is at least an order of magnitude smaller than the T_1 range required to resolve the FT of T_1 for frequency domain maps, according to the Nyquist limit. As discussed above, in the frequency maps, the (ω_1, ω_3) address at which a coherence '*i-j*' will beat along T_2 is given by the values of the $(\omega_i - \omega_{GS})$ and $(\omega_j - \omega_{GS})$ transition frequencies. In the time-frequency measurements discussed here, since only the third time interval T_3 is Fourier transformed, only the addresses of the coherences along ω_3 are resolved. All the intra-band and inter-band *i-j* coherences can be found in traces along T_2 in different ranges of ω_3 but at the same value of T_1. This partial resolution of the addresses of the coherences significantly reduces the number of time delays that need to be sampled to characterize or exploit them for quantum technologies applications.

Modeling of action-based photocurrent response

2DES action-based fluorescence and photocurrent measurements[20-27, 39] are a practical alternative to the polarization BOXCARS ones because they can be implemented with a much simpler collinear set-up.[5] In addition, photocurrent is a more appropriate choice of observable for quantum technology applications as photocurrent measurements can be directly interfaced with classical electronics. Using the phase modulation approach described above, we report here on the computed photocurrent response of electronic coherences of an ensemble of monomeric QDs. We set the pulse parameters so as to access the mono and biexciton states of the QD's and show how electronic coherences involving biexciton states can be characterized in the (T_1, T_2, ω_3) photocurrent action signal in the Double Quantum Coherence (DQC) PMD. Note, while the DQC PMD spectra can be easily measured with a phase modulation set-up[20], such measurements are harder with the BOXCARS set-up because of the lack of fully reliable procedures to correctly phase the signal[43] and the possible contribution of strong spurious nonresonant solvent response[44].

Figure 6 shows the level structure of the mono and bi-excitonic states of a single CdSe QD of 3nm. It comprises the ground state $|0\rangle$, two monoexciton states $|1\rangle$ and $|2\rangle$, the S_1 and the S_2 states and the three biexciton states $|3\rangle$, $|4\rangle$ and $|5\rangle$, which correspond to a double excitation to S_1, to an excitation to S_1 and to S_2, and to a double excitation to S_2, respectively. These 5 excited states are represented by blue horizontal lines on the figure. The horizontal red dashed lines in Figure 6 show the carrier frequency (and twice the carrier frequency) of the laser pulse used to excite the QDs and the allowed dipole transitions are indicated with green vertical arrows. The calculated transition energies between these states averaged over an ensemble of 4000 monomeric QDs with 9% size dispersion, as well as the energies of the coherences between them, are given in Table S3 of the SI along with the corresponding periods and dipole transition moments. Also given are dephasing lifetimes due to the size dispersion.

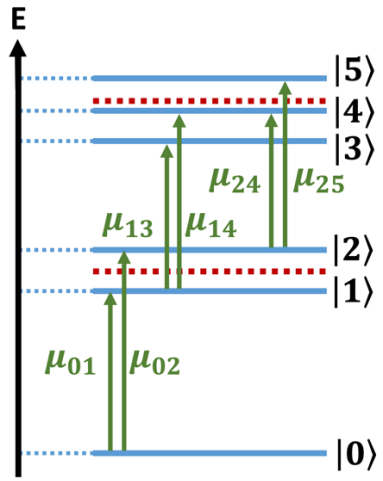

Figure 6: Energy level diagram for excitonic system. The blue lines show the mono- and biexciton electronic states of the QD. The red dashed line shows the carrier frequency (and twice the carrier frequency) of the pulses used in the 2DES.

For the energy bandwidth of the laser pulses used here, the only transitions energetically allowed are those between the GS and the monoexciton band and between the mono and biexciton bands, as shown. Intra-band transitions between the states of the mono or the biexciton bands are not resonant with the laser pulse.

Measurements of incoherent actions signals such as fluorescence or, as we show here, photocurrent, require a setup with 4 pulses.[21-22, 25, 45] The nonlinear signals in specific PMDs are obtained using the phase modulation approach described above.

The experimental setup modelled is shown in Figures 7 (a) and (b).[25] A sequence of L trains of pulses is incident upon the ensemble, each train being constituted of 4 pulses separated in time by the delay times T_1, T_2 and T_3. Each train in the sequence has the same set of delay times, and the trains are spaced apart from one another by the repetition time t_{rep}. The total electric field of each train is the same as in Eq. (3), only the sum runs over n=1, 2, 3 and 4. The action signal, from which the photocurrent is calculated, is recorded along t_{rep}. For a given set of delay times (T_1, T_2, T_3), the carrier envelope phases of the 4 pulses are modulated from $u = 1$ to L. The sequence is repeated using different values of the delay times and so the total photocurrent response is calculated as a function of the delay times and the phase modulation $P_u(T_1, T_2, T_3)$. The total photocurrent is separated into the different PMDs using Eq.(4) and these data are Fourier transformed along T_3, $\mathcal{P}_{PMD}(T_1, T_2, T_3) \leftrightarrow \mathcal{P}_{PMD}(T_1, T_2, \omega_3)$. This post processing produces a cube of data in which the photocurrent response in a specific PMD is stored as a function of T_1, T_2, ω_3, as shown in Figure 7 (c). The analysis of this cube allows to identify and exploit the coherences contributing to this PMD.

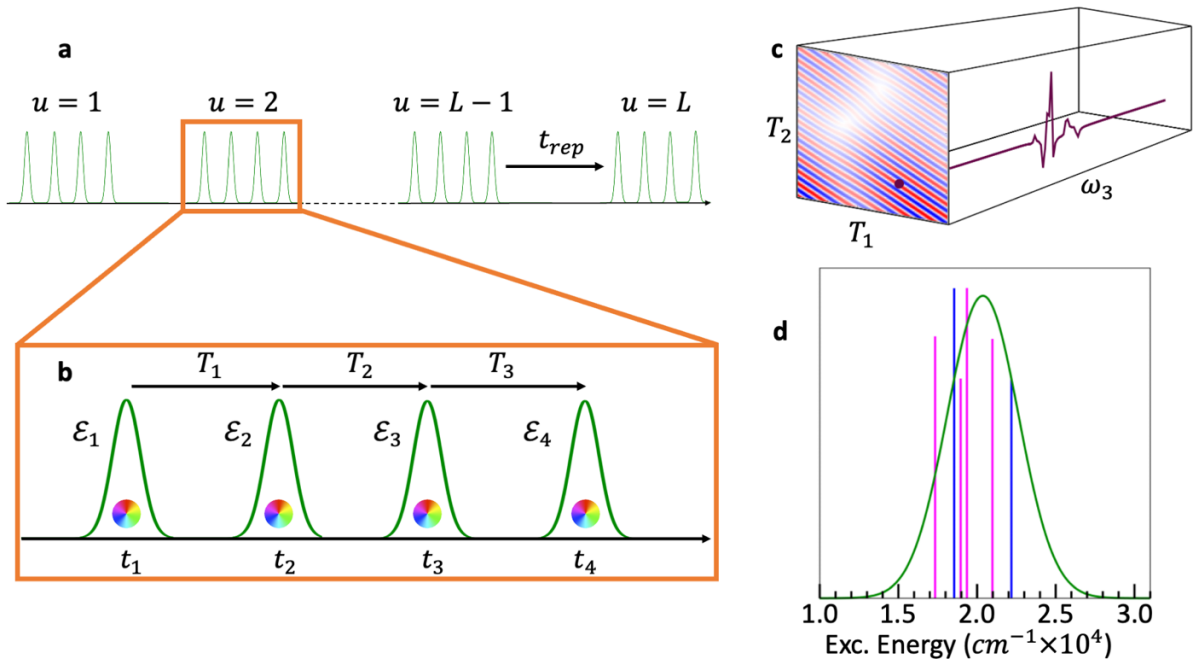

Figure 7: a) Sequence of L phase modulated 4 pulse trains used in the simulation. Each train has a different value of u from 0 to L which modulates the carrier-envelope phase and the trains are spaced by the laser repetition time, t_{rep}. b) The 4 pulses in each train are separated by the delay times, T_1, T_2 and T_3, which are fixed in each sequence of L trains. The measurement is repeated using sequences with different sets of delay times. c) The observable response in a specific PMD stored in a cube of data as a function of T_1, T_2 and ω_3. d) The calculated system stick spectrum with ground state - monoexciton transitions in blue and monoexciton-biexciton transitions in pink. The pulse envelope in the energy domain is superimposed onto the stick spectrum in green.

We take here for the pulse parameters: $\mathcal{E}_0 = 5 \times 10^{-6}$ a.u. (8.775 10^5 W/cm^2), $\omega_n = 2.53$ eV and $\sigma_n = 3.32\, fs$ for $n = 1, 2, 3, 4$. The pulse envelope for these parameters in the energy domain is shown in Figure 7 d), superimposed onto the stick spectrum of the ground-monoexciton and mono-biexciton transitions. In the simulations, $L = 170$, $m_1 = 0$, $m_2 = 2, m_3 = 5$ and $m_4 = 34$.

The observable response being computed is the photocurrent. We take the relaxation time of the biexciton states to the monoexciton states in the sub-picosecond range, and the monoexciton states are assumed to relax to the ground state with a lifetime of a dozen of picoseconds. Consequently, the relaxation time from the $|3\rangle$ and $|5\rangle$ biexciton states to the $|1\rangle$ and $|2\rangle$ monoexciton is fixed to be 318 fs, with corresponding rates $\Gamma_{3\to1} = \Gamma_{5\to2} = 1.3 \times 10^{-2}\, eV$. The relaxation time from the $|4\rangle$ biexciton state to the $|1\rangle$ and $2\rangle$ monoexciton states is taken to be a little longer, 636 fs, with corresponding width in energy $\Gamma_{4\to1} = \Gamma_{4\to2} = 6.5 \times 10^{-3}\, eV$. The relaxation time from the $|1\rangle$ and $|2\rangle$ monoexciton states to the $|0\rangle$ ground state is taken to be 15.9 ps, with corresponding width $\Gamma_{1\to0} = \Gamma_{2\to0} = 2.6 \times 10^{-4}\, eV$.

The total photocurrent response is calculated from the density matrix of the ensemble using the approximated Liouvillian given in Eq. (6) to which we added the relaxation rates defined above. Additionally, a decay term was added to the Liouvillian to account for the dephasing of the coherences caused by phonon coupling with strength $\gamma = 0.005\, eV$. Both the relaxation of the biexciton to the monoexciton states and of the monoexciton states to the ground state contribute to the photocurrent signal.[22, 45] The action signal response from the relaxation of state $|m\rangle$ to state $|n\rangle$ is computed as [33]:

$$Resp_{mn} = \int_{t_4}^{t_{aquisition}} dt\, \Gamma_{mn} Tr[|n\rangle\langle m|\rho(t)|m\rangle\langle n|] \quad (11)$$

The integral of Eq. (11) is evaluated along the acquisition time of the experiment which runs from the time of the fourth pulse in the sequence over the repetition time to the next sequence, t_{rep}, as shown in Figure 7 (a). In the simulations, t_{rep} is approximated as ∞ since it is much longer than all the relaxation processes of the mono- and biexciton states to the ground state.

The total action signal response

$$Resp = \int_{t_4}^{t_{aquisition}} dt \sum_{m,n} \Gamma_{mn}\, Tr[|n\rangle\langle m|\rho(t)|m\rangle\langle n|] \quad (12)$$

The total photocurrent calculated from Eq. (12) is separated into its non-linear phase matching components by Fourier transforming along the phase modulations, Eq. (4). We report here on the double quantum component, DQC, PMD: $DQC = m_4 + m_3 - m_2 - m_1$. As explained before, this is a phase matching direction challenging to be reliably measured in the BOXCARS set-up, yet very appealing to quantify shifts of the energy correlation between two monoexcitons, in particular to study many-body effects and excited-state landscapes in a wide range of systems including biomolecules and inorganic materials.[19-20, 46-48]

The calculated cube of data is then converted into the time-frequency domain by Fourier transforming along $\mathcal{P}_{DQC}(T_1, T_2, T_3) \leftrightarrow \mathcal{P}_{DQC}(T_1, T_2, \omega_3)$.

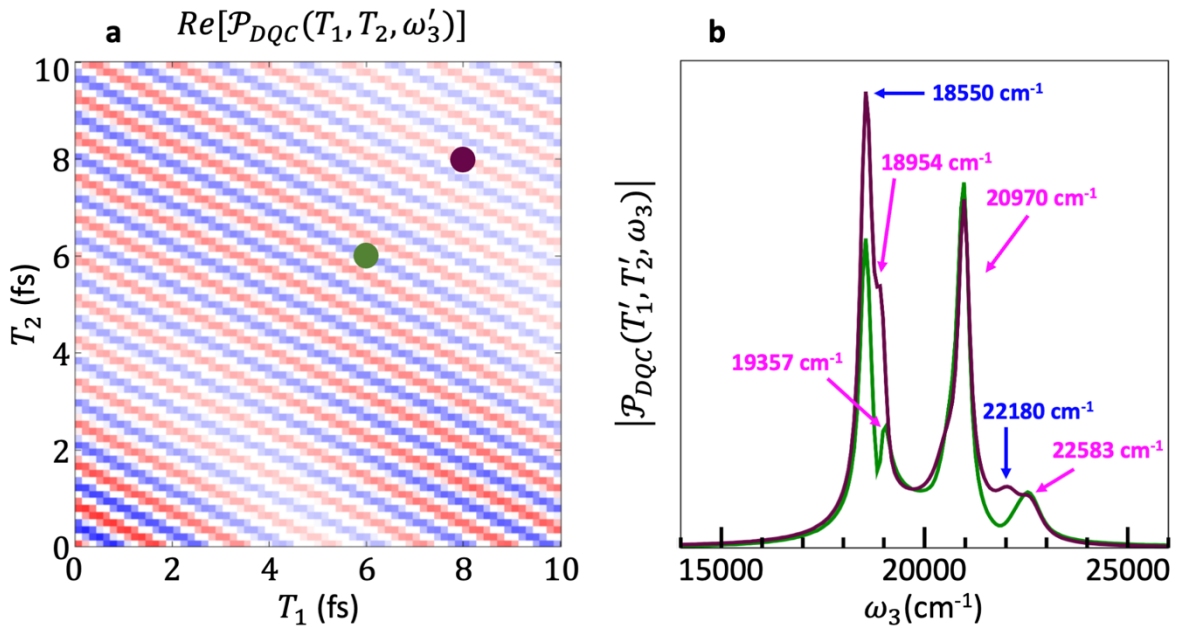

Figure 8: a) (T_1, T_2) Time map of the real part of the photocurrent response in the DQC PMD for a value of $\omega_3 = 20000\ cm^{-1}$. b) Traces along ω_3 at the points indicated on a) with a green dot, (T_1, T_2)= $(6.0\ fs, 6.0\ fs)$ and a burgundy dot, (T_1, T_2)= $(8.0\ fs, 8.0\ fs)$. The signal corresponding to ground-monoexciton state coherences is identified with blue arrows, the signal corresponding to mono-biexciton state coherences is identified with pink arrows.

Figure 8 (a) shows a (T_1, T_2) time map of the real part of the photocurrent response in the DQC PMD for a value of $\omega_3 = 20000\ cm^{-1}$. The pathways contributing to the DQC PMD using a third order perturbative approach are enumerated as double-sided Feynman diagrams by Damtie et al.[45]. We do not use a perturbative approach here, instead computing the photocurrent response from the dynamics of the density matrix (Eq. (6)). However, the pulse strength used in the simulation is sufficiently weak that the third order perturbative treatment is a good approximation of the exact time-dependent response and provides good insights into the excitation pathways contributing to the signal. The double-sided Feynman diagrams which contribute to the DQC PMD all have in common that the first pulse excites the ket from the ground state to a monoexciton state, and the second pulse excites this ket from the monoexciton state to a biexciton state. This means that for the duration of T_1 the system will be in a coherence between the ground state and a monoexciton state, and that for the duration of T_2 the system will be in a coherence between the ground state and a biexciton state. These features clearly appear in the time map of Figure 8 (a). If one compares the number of oscillations along the T_1 axis to those along the T_2 axis, it is clear that there are more beatings in the same time along T_2 than T_1, this reflects the fact that the ground-biexciton coherences have much shorter periods, about twice shorter, than the ground-monoexciton coherences (see Table S3).

Figure 8 (b) shows the absolute values of the traces along ω_3 of two points on the (T_1, T_2) time map. The Feynman diagrams[45] show that the third pulse in the train can either relax the ket from the biexciton state to a mono-exciton state or excite the bra from the ground state to a mono-exciton state. This means that for the duration of T_3 the system can either be in a coherence between the ground and a monoexciton state or between a monoexciton and a biexciton state. This is shown in Figure 8 (b), on which the fast beating responses corresponding to ground-mono as well as ground-bi coherences are identified.

Note that the signal of the two traces plotted on Figure 8 (b), while being dominated by the same primary frequencies, differs in the specific coherences which can be identified. This small but important variability of the coherences in the ω_3 traces of different (T_1, T_2) points means that a comprehensive collection of coherence data still requires repetitions for a small number of T_1 and T_2 values, albeit far fewer than would be needed if Fourier transforms along these delay times were required. In addition to the inhomogeneous broadening resulting from the size dispersion of the ensemble, the peaks in Figure 8 (b) are broaden by the coupling to the phonon modes.

The analysis of the computed photocurrent response in an additional PMD, the DQC PMD, shows that coherences involving biexciton states can be observed in the action signal photocurrent response of QD ensembles to 2DES. As in the case of the polarization response, directly measured data in the (T_1, T_2, ω_3) domain are usable without the need for additional post-processing Fourier transforms along T_1 and T_2. A sampling of the delay time, T_3, for fixed values of T_1 and T_2 enables one to characterize all the coherences found in the pathways contributing to the DQC PMD. This, in turn, means that fewer measurements along these delay times are needed. Furthermore, these results show that the (T_1, T_2, ω_3) is the appropriate domain for looking at coherences in observables in the DQC PMD.

Conclusions

We have shown that the electronic coherences resulting from the excitation of ensembles of size-dispersed QD's and QD dimers by sequences of fs broad bandwidth laser pulses, as in 2DES, can be observed and characterized in the directly measured time-frequency domain. We have shown that this is the case for both polarization and action-based, here photocurrent,

measurements. For the case of a cube of data that depends on three delay times, we show that the electronic coherences are characterized by robust and distinct beating patterns in the traces of the signal as a function of one delay time at a single point in the time-frequency domain of the other two delay times. In the case of polarization measurements, we get very good agreement between the modeled and experimental (T_1, ω_3) time-frequency maps in the rephasing PMD, and in T_2/ω_2 traces along these maps.

Compared to the conventional (ω_1, ω_3) frequency maps, the advantage of directly exploiting time-frequency data leads to a considerable reduction of the number of time intervals that need to be sampled. The reason is that in a time-frequency map, the addresses of the coherences are only partially resolved. All the coherences between excited states *i* and *j,* which have a common state *j,* beat in the traces of points with the same T_1 value. By fixing ω_3 to be within the inhomogeneous broadening of the transition *j* to the GS, and recording a trace at a point (T_1, ω_3) along T_2, one can characterize in one go all the beating frequencies of a family of coherences that involve the same emitting state *j* in the chosen PMD because the absorbing states *i* are not resolved along T_1.

That several coherences are accessible simultaneously in the directly measured time-frequency domain is a huge advantage for the exploitation of QD electronic coherences in quantum technologies for parallel information processing. The savings in fewer measurements and less computation time will greatly enhance the advantage of logical operations encoded onto coherences over classical logic operations. Action-based photocurrent measurements of electronic coherences are a step further in coherence exploitation since they open the way for QD devices to be integrated into classical architectures.

Supporting Information is available at ….

Acknowledgement

The work of JRH and FR is supported by the Fonds National de la Recherche, F.R.S. – FNRS (Belgium), #T.0205.20. Computational resources have been provided by the Consortium des Equipements de Calcul Intensif (CECI), funded by the F.R.S.-FNRS under Grant # 2.5020.11. EC acknowledges partial support by "CQ-TECH" Supporting Talent in Research@University of Padova (STARS) Grant 2019 (2019-UNPD0Z9- 0166571). The Authors thank Dr. Rosaria Brescia of the Italian Institute of Technology for the high-resolution TEM image in Fig. 1b and Hugo Gattuso for discussions on the modeling of the electronic structure of the QDs.

References

1. Rebentrost, P.; Stopa, M.; Aspuru-Guzik, A., Förster Coupling in Nanoparticle Excitonic Circuits. *Nano Lett.* **2010**, *10*, 2849-2856.
2. Spittel, D.; Poppe, J.; Meerbach, C.; Ziegler, C.; Hickey, S. G.; Eychmüller, A., Absolute Energy Level Positions in Cdse Nanostructures from Potential-Modulated Absorption Spectroscopy (Emas). *ACS Nano* **2017**, *11*, 12174-12184.
3. Kagan, C. R.; Bassett, L. C.; Murray, C. B.; Thompson, S. M., Colloidal Quantum Dots as Platforms for Quantum Information Science. *Chem. Rev.* **2021**, *121*, 3186-3233.

4. Koley, S.; Cui, J.; Panfil, Y. E.; Banin, U., Coupled Colloidal Quantum Dot Molecules. *Acc. Chem. Res.* **2021**, *54*, 1178-1188.
5. Collini, E., 2d Electronic Spectroscopic Techniques for Quantum Technology Applications. *J. Phys. Chem. C* **2021**, *125*, 13096-13108.
6. Dibenedetto, C. N., et al., Coupling in Quantum Dot Molecular Hetero-Assemblies. *Mater. Res. Bull.* **2022**, *146*, 111578.
7. Hamilton, J. R.; Amarotti, E.; Dibenedetto, C. N.; Striccoli, M.; Levine, R. D.; Collini, E.; Remacle, F., Harvesting a Wide Spectral Range of Electronic Coherences with Disordered Quasi-Homo Dimeric Assemblies at Room Temperature. *Advanced Quantum Technologies* **2022**, *n/a*, 2200060.
8. Gattuso, H.; Levine, R. D.; Remacle, F., Massively Parallel Classical Logic Via Coherent Dynamics of an Ensemble of Quantum Systems with Dispersion in Size. *Proc. Natl. Acad. Sci. USA* **2020**, *117*, 21022.
9. Komarova, K.; Gattuso, H.; Levine, R. D.; Remacle, F., Quantum Device Emulates the Dynamics of Two Coupled Oscillators. *J. Phys. Chem. Lett.* **2020**, *11*, 6990-6995.
10. Komarova, K.; Gattuso, H.; Levine, R. D.; Remacle, F., Parallel Quantum Computation of Vibrational Dynamics. *Front. Phys.* **2020**, *8*, 486.
11. Remacle, F.; Levine, R. D., A Quantum Information Processing Machine for Computing by Observables. *ChemRxiv* **2022**.
12. Fresch, B.; Hiluf, D.; Collini, E.; Levine, R. D.; Remacle, F., Molecular Decision Trees Realized by Ultrafast Electronic Spectroscopy. *Proc. Natl. Acad. Sci. USA* **2013**, *110*, 17183-17188.
13. Collini, E.; Gattuso, H.; Levine, R. D.; Remacle, F., Ultrafast Fs Coherent Excitonic Dynamics in Cdse Quantum Dots Assemblies Addressed and Probed by 2d Electronic Spectroscopy. *J. Chem. Phys.* **2021**, *154*, 014301.
14. Collini, E.; Gattuso, H.; Bolzonello, L.; Casotto, A.; Volpato, A.; Dibenedetto, C. N.; Fanizza, E.; Striccoli, M.; Remacle, F., Quantum Phenomena in Nanomaterials: Coherent Superpositions of Fine Structure States in Cdse Nanocrystals at Room Temperature. *J. Phys. Chem. C* **2019**, *123*, 31286-31293.
15. Collini, E., et al., Room-Temperature Inter-Dot Coherent Dynamics in Multilayer Quantum Dot Materials. *J. Phys. Chem. C* **2020**, *124*, 1622-16231.
16. Gelzinis, A.; Augulis, R.; Butkus, V.; Robert, B.; Valkunas, L., Two-Dimensional Spectroscopy for Non-Specialists. *Biochimica et Biophysica Acta (BBA) - Bioenergetics* **2019**, *1860*, 271-285.
17. Brańczyk, A. M.; Turner, D. B.; Scholes, G. D., Crossing Disciplines - a View on Two-Dimensional Optical Spectroscopy. *Annalen der Physik* **2014**, *526*, 31-49.
18. Hybl, J. D.; Albrecht, A. W.; Gallagher Faeder, S. M.; Jonas, D. M., Two-Dimensional Electronic Spectroscopy. *Chem. Phys. Lett.* **1998**, *297*, 307-313.
19. Bolzonello, L.; Volpato, A.; Meneghin, E.; Collini, E., Versatile Setup for High-Quality Rephasing, Non-Rephasing, and Double Quantum 2d Electronic Spectroscopy. *J. Opt. Soc. Am. B* **2017**, *34*, 1223-1233.
20. Mueller, S.; Draeger, S.; Ma, X.; Hensen, M.; Kenneweg, T.; Pfeiffer, W.; Brixner, T., Fluorescence-Detected Two-Quantum and One-Quantum–Two-Quantum 2d Electronic Spectroscopy. *J. Phys. Chem. Lett.* **2018**, *9*, 1964-1969.
21. Bakulin, A. A.; Silva, C.; Vella, E., Ultrafast Spectroscopy with Photocurrent Detection: Watching Excitonic Optoelectronic Systems at Work. *J. Phys. Chem. Lett.* **2016**, *7*, 250-258.
22. Karki, K. J.; Widom, J. R.; Seibt, J.; Moody, I.; Lonergan, M. C.; Pullerits, T.; Marcus, A. H., Coherent Two-Dimensional Photocurrent Spectroscopy in a Pbs Quantum Dot Photocell. *Nat. Commun* **2014**, *5*, 5869.

23. Nardin, G.; Autry, T. M.; Silverman, K. L.; Cundiff, S. T., Multidimensional Coherent Photocurrent Spectroscopy of a Semiconductor Nanostructure. *Opt. Express* **2013**, *21*, 28617-28627.
24. Bian, Q., et al., Vibronic Coherence Contributes to Photocurrent Generation in Organic Semiconductor Heterojunction Diodes. *Nat. Commun* **2020**, *11*, 617.
25. Bolzonello, L.; Bernal-Texca, F.; Gerling, L. G.; Ockova, J.; Collini, E.; Martorell, J.; van Hulst, N. F., Photocurrent-Detected 2d Electronic Spectroscopy Reveals Ultrafast Hole Transfer in Operating Pm6/Y6 Organic Solar Cells. *J. Phys. Chem. Lett.* **2021**, *12*, 3983-3988.
26. Bruschi, M.; Gallina, F.; Fresch, B., Simulating Action-2d Electronic Spectroscopy of Quantum Dots: Insights on the Exciton and Biexciton Interplay from Detection-Mode and Time-Gating. *Phys. Chem. Chem. Phys.* **2022**.
27. Karki, K. J.; Ciappina, M. F., Advances in Nonlinear Spectroscopy Using Phase Modulated Light Fields: Prospective Applications in Perturbative and Non-Perturbative Regimes. *Advances in Physics: X* **2022**, *7*, 2090856.
28. Dibenedetto, C. N., et al., Coupling Effects in Qd Dimers at Sub-Nanometer Interparticle Distance. *Nano Res.* **2020**, *13*, 1071-1080.
29. Irgen-Gioro, S.; Spencer, A. P.; Hutson, W. O.; Harel, E., Coherences of Bacteriochlorophyll a Uncovered Using 3d-Electronic Spectroscopy. *J. Phys. Chem. Lett.* **2018**, *9*, 6077-6081.
30. Luttinger, J. M.; Kohn, W., Motion of Electrons and Holes in Perturbed Periodic Fields. *Phys. Rev.* **1955**, *97*, 869-883.
31. Brus, L., Electronic Wave Functions in Semiconductor Clusters: Experiment and Theory. *J. Phys. Chem.* **1986**, *90*, 2555-2560.
32. Zunger, A., Electronic Structure Theory of Semiconductor Quantum Dots. *MRS Bulletin* **1998**, 35-42.
33. Efros, A. L.; Rosen, M., The Electronic Structure of Semi-Conducting Nanocrystal. *Ann. Rev. Mater. Sci.* **2000**, *30*, 475-521.
34. Righetto, M.; Bolzonello, L.; Volpato, A.; Amoruso, G.; Panniello, A.; Fanizza, E.; Striccoli, M.; Collini, E., Deciphering Hot- and Multi-Exciton Dynamics in Core–Shell Qds by 2d Electronic Spectroscopies. *Phys. Chem. Chem. Phys.* **2018**, *20*, 18176-18183.
35. Efros, A. L.; Rosen, M.; Kuno, M.; Nirmal, M.; Norris, D. J.; Bawendi, M., Band-Edge Exciton in Quantum Dots of Semiconductors with a Degenerate Valence Band: Dark and Bright Exciton States. *Phys. Rev. B* **1996**, *54*, 4843-4856.
36. Norris, D. J.; Bawendi, M. G., Measurement and Assignment of the Size-Dependent Optical Spectrum in Cdse Quantum Dots. *Phys. Rev. B* **1996**, *53*, 16338-16346.
37. Wong, C. Y.; Scholes, G. D., Using Two-Dimensional Photon Echo Spectroscopy to Probe the Fine Structure of the Ground State Biexciton of Cdse Nanocrystals. *J. Lumin.* **2011**, *131*, 366-374.
38. Kjellberg, P.; Brüggemann, B.; Pullerits, T., Two-Dimensional Electronic Spectroscopy of an Excitonically Coupled Dimer. *Phys. Rev. B* **2006**, *74*, 024303.
39. Draeger, S.; Roeding, S.; Brixner, T., Rapid-Scan Coherent 2d Fluorescence Spectroscopy. *Optics Express* **2017**, *25*, 3259-3267.
40. Nardin, G. A., T. M.; Silverman, K. L.; Cundiff, S. T., Multidimensional Coherent Photocurrent Spectroscopy of a Semiconductor Nanostructure. *Opt. Express* **2013**, *21*, 28617.
41. Calhoun, T. R.; Ginsberg, N. S.; Schlau-Cohen, G. S.; Cheng, Y.-C.; Ballottari, M.; Bassi, R.; Fleming, G. R., Quantum Coherence Enabled Determination of the Energy Landscape in Light-Harvesting Complex Ii. *J. Phys. Chem. B* **2009**, *113*, 16291-16295.
42. Mork, A. J.; Lee, E. M. Y.; Tisdale, W. A., Temperature Dependence of Acoustic Vibrations of Cdse and Cdse–Cds Core–Shell Nanocrystals Measured by Low-Frequency Raman Spectroscopy. *Phys. Chem. Chem. Phys.* **2016**, *18*, 28797-28801.

43. Nemeth, A.; Milota, F.; Mančal, T.; Pullerits, T.; Sperling, J.; Hauer, J.; Kauffmann, H. F.; Christensson, N., Double-Quantum Two-Dimensional Electronic Spectroscopy of a Three-Level System: Experiments and Simulations. *J. Chem. Phys.* **2010**, *133*, 094505.
44. Gellen, T. A.; Bizimana, L. A.; Carbery, W. P.; Breen, I.; Turner, D. B., Ultrabroadband Two-Quantum Two-Dimensional Electronic Spectroscopy. *J. Chem. Phys.* **2016**, *145*, 064201.
45. Damtie, F. A.; Wacker, A.; Pullerits, T.; Karki, K. J., Two-Dimensional Action Spectroscopy of Excitonic Systems: Explicit Simulation Using a Phase-Modulation Technique. *Phys. Rev. A* **2017**, *96*, 053830.
46. Kim, J.; Mukamel, S.; Scholes, G. D., Two-Dimensional Electronic Double-Quantum Coherence Spectroscopy. *Acc. Chem. Res.* **2009**, *42*, 1375-1384.
47. Stone, K. W.; Gundogdu, K.; Turner, D. B.; Li, X.; Cundiff, S. T.; Nelson, K. A., Two-Quantum 2d Ft Electronic Spectroscopy of Biexcitons in Gaas Quantum Wells. *Science* **2009**, *324*, 1169.
48. Christensson, N.; Milota, F.; Nemeth, A.; Pugliesi, I.; Riedle, E.; Sperling, J.; Pullerits, T.; Kauffmann, H. F.; Hauer, J., Electronic Double-Quantum Coherences and Their Impact on Ultrafast Spectroscopy: The Example of B-Carotene. *J. Phys. Chem. Lett.* **2010**, *1*, 3366-3370.